CO_2 Snow Fall on Mars: Simulation with a General Circulation Model

François Forget, Frédéric Hourdin and Olivier Talagrand

Laboratoire de Météorologie Dynamique du CNRS,
Université Paris 6, BP99, 75252 Paris Cedex 05, FRANCE
Fax: (33)1 44 27 62 72   Phone: (33)1 44 27 47 63
E-mail : forget@lmd.ens.fr

Icarus 131, 302-316 (1998)

Although CO_2 snow-fall has never been directly observed on Mars, it has been suggested that such precipitation may explain the puzzling infrared measurements obtained by Mariner 9 and Viking during the polar night in each hemisphere. The radiative effect of the snow would strongly alter the radiative balance of the condensing polar caps and thus the CO_2 cycle and the global climate. We have simulated this phenomenon with a General Circulation Model (GCM). For that purpose, a new parametrisation of CO_2 condensation in the atmosphere and on the ground has been developed, paying particular attention to mass and energy conservation, and allowing for the possible sublimation of sedimenting CO_2 ice particles. Atmospheric condensation may result from radiative cooling on the one hand (especially when the atmosphere is dust laden), and from adiabatic cooling in upward motions on the other hand. This latter process can be very efficient locally. On this basis, we have modeled the effect of the CO_2 snow-fall on the infrared emission by decreasing the local emissivities when atmospheric condensation was predicted by the model. This parametrization is based on physical considerations (radiative transfer through the CO_2 ice particles, snow metamorphism on the ground). Without tuning the model parameters, we have been able to accurately reproduce the general behavior of the features observed by Viking in the thermal infrared. These modeling results support the CO_2 snow fall scenario suggested from the observations. Overall, this new parameterization, used in combination with the Digital Terrain Model (DTM) topography and with allowance for a varying atmospheric dust content, allows the GCM to simulate the CO_2 condensation-sublimation cycle realistically. In particular, the seasonal variations of the surface pressure recorded by the Viking Landers can now be reproduced without artificially decreasing the condensation rate as was done in previous studies.

1 Introduction

Every Martian year, as much as 30% of the CO_2 atmosphere of Mars condenses in the polar caps of each hemisphere during their respective polar nights. The formation of the Martian polar caps have been studied with numerous numerical models, starting with the thermal model designed by Leighton and Murray (1966) who originally predicted the existence of the Martian CO_2 cycle. Recent modeling efforts include more sophisticated energy balance models (e.g. James and North 1979, Wood and Paige 1992, Pollack *et al.* 1993a) and climate simulation with general circulation models or GCMs (Pollack *et al.* 1981, 1990, Hourdin *et al.* 1993, 1995). Unlike the energy balance models which usually assume that the CO_2 directly condenses on the ground, GCMs can estimate the amount of CO_2 condensing in the atmosphere. For instance, Pollack *et al.* (1990) showed that a fraction of the total CO_2 condensation could take place in the atmosphere, especially when the atmosphere is dust laden because of the increased atmospheric emissivity. However, in every GCM study so far, the condensed CO_2 has been assumed to precipitate instantaneously to the surface without changing the properties of the atmosphere and the cap.

The available observations of the condensing polar caps suggest that reality may be more complex. The IRTM instrument aboard Viking measured 20-μm brightness temperatures showing considerable structures with anomalously low values in the winter polar regions (Kieffer *et al.* 1976), far below 148 K, the temperature appropriate for condensed carbon dioxide in vapor pressure equilibrium at the expected atmospheric pressure. The location and brightness temperatures of these areas (hereafter also called "low emission zones") sometimes varied on timescales of days (Kieffer *et al.* 1977). The low emission zones were also characterized by a complex spectral signature as observed by Mariner 9 IRIS (Paige *et al.* 1990). Various scenarios have been suggested to explain these observations, including the effect of CO_2 ice clouds (see Kieffer *et al.* 1977, Hunt 1980, Paige 1985). Recently, Forget *et al.* (1995) showed that these low emission zones were likely to be created by the radiative properties of CO_2 snow falls (falling snow particles or fresh snow deposits). In this scenario, the infrared emission is decreased because the CO_2 ice particles that condense in the atmosphere can be efficient scatterers at infrared wavelengths (whether they are airborne or have just fallen to the ground) whereas CO_2 ice deposits composed of non-porous solid ice having directly condensed on the ground or having undergone frost metamorphism should behave almost like blackbody emitters, or, more likely, be transparent in the infrared so that the ground beneath can radiate through.

Such processes affecting the radiative balance of the polar regions are likely to have a strong impact on the CO_2 condensation rate. In a subsequent analysis of the Viking thermal infrared observations of the condensing polar caps, Forget and Pollack (1996) estimated that the total condensation rate was decreased by 10 to 20% in the polar regions during the winter, especially in the northern hemisphere.

In this paper, our purpose is to simulate CO_2 snowfall and its radiative effects with the LMD General Circulation Model. The interest is twofold. On the one hand, the GCM provides an excellent tool to study, simulate and validate the CO_2 snow fall scenario derived from the observations. On the other hand, an accurate description of polar processes in a GCM allows us to compute the seasonal variation of the global atmospheric pressure due to the CO_2 cycle.

In section 2, we give a brief description of the LMD General Circulation Model, with a particular emphasis on a new CO_2 condensation-sublimation scheme developed for the present study (a numerical expression of the scheme is given in the appendix). In section 3, we analyze the processes which control condensation in the atmosphere and lead to CO_2 snow fall. In section 4, we propose a simple parametrisation of the radiative effects of falling snow particles or fresh snow deposits. This parametrisation allows us to simulate the low emission zones observed by Viking. A detailed comparison of the modeled features with the observations is presented. In section 5, we show that this new parametrization allows us to realistically simulate the global seasonal CO_2 cycle without artificially decreasing the condensation rate as was done previously.

2 The LMD General Circulation Model

2.1 Main characteristics

The LMD Martian GCM employed for the simulation has been described by Hourdin *et al.* (1993, 1995). It is a finite difference model based on the primitive equations of meteorology in σ coordinates, where $\sigma = p/p_s$ is the pressure normalized by its local value at the surface. The resolution used for the present study is 64×48 horizontally, corresponding to 3.75^o latitude by 5.625^o longitude, and 25 vertical layers. The middle of the first 3 layers are at about 3.5, 16, and 40 m whereas the middle of the top layer is around 95 km.

Since 1995, a number of enhancements have been made to the "physical" part of the model which includes the radiative transfer calculations, the subgrid scale dynamical processes and the surface processes. These changes will be the subject of a future publication. We give here only a brief overview of the version of the model that was used for the study.

In the thermal infrared, the radiative transfer code now accounts for scattering by the dust, in addition to absorption and emission. The treatment of the dust is based on the algorithm developed by Toon *et al.* (1989). The absorption and emission by carbon dioxide is still computed using the code developed by Hourdin (1992). At solar wavelengths, besides dust absorption and scattering, we have included a simple parametrisation for the computation of near infrared heating by the CO_2 gas, which is negligible below 30 km but becomes considerable above 50 km. The dust optical properties were derived from Ockert-Bell *et al.* (1997) at solar wavelengths, and from an "improved" version of the Toon *et al.* (1977) model in the infrared. Following Martin (1986) and Clancy *et al.* (1995), the visible (0.67 μm) to infrared (9 μm) dust optical depth ratio which is tunable in the model has been set to 2.

The formulation of the vertical turbulent mixing (mainly of importance in the planetary boundary layer) has been improved based on a non-stationary Mellor and Yamada (1974) type second order closure scheme. In addition to this parametrization, a convective adjustment scheme is used to prevent subadiabatic vertical temperatures gradients. The temperature of the surface is computed from the radiative, sensible and latent heat fluxes at the surface using an 11-level model of thermal diffusion in the soil. Surface properties, i.e. albedo and thermal inertia, are based on the Viking observations analyzed by Pleskot and Miner (1982) and Palluconi and Kieffer (1981), completed in the polar regions by the recent results from Paige *et al.* (1994) and Paige and Keegan (1994). Unlike Hourdin *et al.* (1993, 1995), we have used the USGS Digital Elevation Map (often called DTM) for the topography.

2.2 CO_2 condensation-sublimation scheme

This particular scheme has been entirely revised for the present study. Here we describe how the condensation and sublimation of CO_2 on the ground and in the atmosphere are now calculated in the model, and which assumption are made. A numerical expression of the condensation-sublimation scheme is given in the appendix.

The condensation and sublimation of carbon dioxide on the ground is primarily controlled by relatively simple physical processes. When the surface temperature falls below the condensation temperature, CO_2 condenses, releasing the latent heat required to keep the solid-gas interface at the condensation temperature. Conversely, when CO_2 ice is heated, it partially sublimes to keep its temperature at the frost point temperature.

In the atmosphere, things are, in theory, more complex. The condensation of a gas involves various microphysical processes: supersaturation, nucleation, crystal growth, sedimentation, etc... On Earth, such processes control the formation of the clouds. They have to be taken into account in General Circulation Models. On Mars, what should we take into account ? First, temperatures colder than the solid-gas equilibrium temperature (supersaturation) may be required to form (nucleation) the condensed particles from the vapor phase. However, on Mars, nucleation is probably facilitated by the presence of airborne dust particles which can serve as condensation nuclei (heterogeneous nucleation). In such conditions, preliminary studies conducted with microphysical models by Wood *et al.* (1996) and Stansberry *et al.* (1995) indicate that, in terms of temperature, the supersaturation required to form CO_2 ice particles in a CO_2 atmosphere is negligible. Thus, we assume that condensation occurs as soon as the temperature reaches the frost point.

For a given condensation rate, the number of particles, their sizes and their rates of sedimentation depend upon numerous and poorly known parameters such as the number of nuclei available, or the finite rate at which CO_2 molecules can be incorporated into the crystal lattice. It must be noted that CO_2 crystals growing in a CO_2 atmosphere present a totally different regime than water ice clouds particles on Earth (Rossow 1978). The growth of water clouds particles on Earth is limited by both the diffusion of water vapor though air and the thermal diffusion of latent heat of condensation away from the particle, whereas the mass diffusion effect is entirely absent in CO_2 ice clouds. Thus for equal supersaturations, CO_2 ice cloud particles should grow faster than the corresponding water ice particles (Pierrehumbert and Erlick 1997). In the model, until more data and model results become available, we have made the following assumption : after condensing at a given level, the CO_2 ice falls through the atmospheric layers located below it down to the ground within a model timestep. In reality, the ice particles fall more slowly and may be horizontally advected by the wind. However, since the atmosphere keeps condensing (the atmosphere is usually supersaturated down to the surface), and this preferentially on the CO_2 ice already formed, the particle size should readily increase. Because the sedimentation velocity is proportional to the square of the particles radius (Stokes' law), it is unlikely that the CO_2 ice may be transported over significant distances. For instance, Wood *et al.*

(1996) estimated that the particle size near the surface should be at least 100 μm, corresponding to a sedimentation velocity larger than 1.4 m s^{-1} (see Table 1, Forget *et al.* 1995). Since the radiative properties of the clouds are taken into account independently (see below), our assumption should not affect the condensation rate on the ground and in the atmosphere. Therefore, the calculation of the condensation rate in the atmosphere is reduced to an of energy and mass budget, similar to the ground case. In the original version of the general circulation model, the CO_2 ice condensing in the atmosphere was simply included in the mass budget of the surface, without taking into account its altitude, its initial temperature and the layers through which it fell. We have since found that this approximation can lead to errors of several percent on the total amount of CO_2 condensed seasonally in the polar caps. The error on the part condensing in the atmosphere was especially large. Thus, we have re-addressed this issue more carefully, with particular attention to mass and energy balances. We now allow for the possible sublimation of sedimenting CO_2 ice particles in warmer atmospheric layers as they descend to the ground. Minor components of the energy budget are included (e.g. the release of potential energy by CO_2 ice particles during their fall, and the heat consumption to warm the particles as the CO_2 frost temperature increases with the local pressure). Also, we have included a correction to account for the mass, heat and momentum redistribution between the model layers due to condensation (see appendix). Last, the boundary layer scheme has been modified so that the turbulent atmospheric mixing takes into account the fact that the atmosphere can never be colder than the CO_2 frost point.

3 Atmospheric condensation

What kind of mechanisms can lead to the condensation of the atmosphere, and thus to CO_2 snow fall ? In this section, we analyse the various processes which lead to cooling and, in turn, condensation of the atmosphere.

3.1 Radiative cooling

In the polar night, the radiative budget of a surface + atmosphere column is reduced to a cooling due to the emission of infrared radiation. Once the ground is cooled to the frost point value, the surface temperature is kept constant by the latent heat released by surface condensation. The atmosphere is then radiatively warmed by the infrared emission from the surface. In fact, as first pointed out by Gierash and Goody (1968) and later by Paige (1985), the corresponding radiative equilibrium is always colder than the condensation temperature profile. Thus, an isolated atmospheric column somewhere in the polar night would rapidly cool and condense out. The latent heat release by the condensation would then balance the radiative cooling to keep the temperature at the frost point value everywhere in the atmosphere.

We have simulated this situation using a 1D version of the GCM radiative transfer code with 25 layers. In such conditions, the cooling rates and the corresponding condensation rate only depends on the radiative properties (emissivity, transmitivity) of the ground and the atmosphere. Fig. 1a shows some cooling and condensation rates obtained for various dust optical depths τ and ground emissivities ε. The correspond-

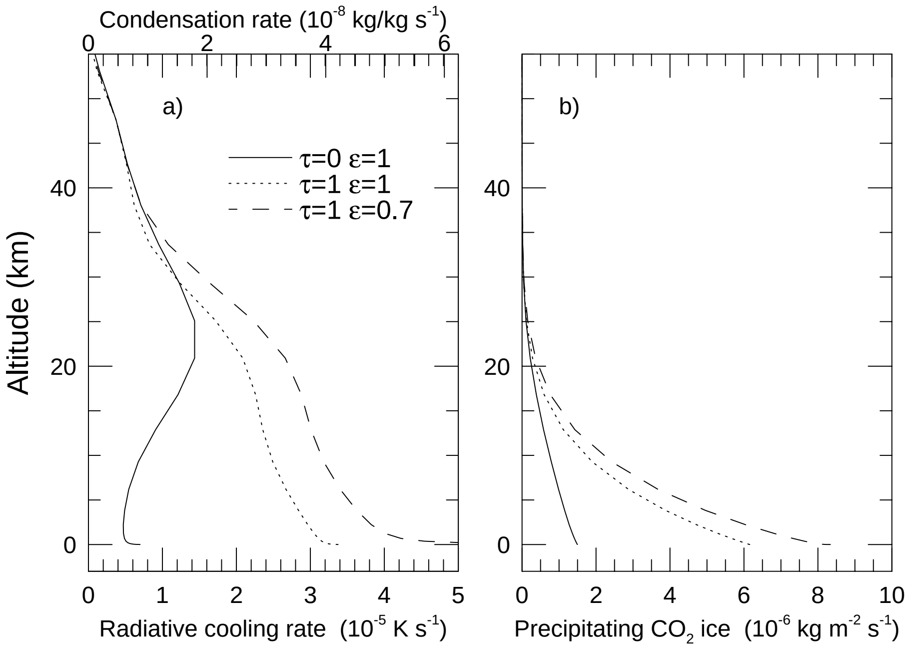

Figure 1: Radiative cooling rate, and corresponding condensation rate and integrated ice precipitation computed for an isolated atmospheric column in the Martian polar night (surface pressure : 700 Pa). Results are shown for different values of the dust optical depth τ and grey emissivity of the surface ε. The temperature is fixed to the condensation temperature everywhere.

ing amount of CO_2 snow falling through the atmosphere at a given level is shown Fig. 1b. The amount of CO_2 condensing in the atmosphere because of radiative cooling is lowest for a clear atmosphere ($\tau = 0$) above a blackbody surface (ε=1). The cooling rate is maximum at 20-25 km altitude. The total rate of condensation in the atmosphere is 1.5 10^{-6} kg m^{-2} s^{-1}, to be compared with the rate of condensation on the ground, 4.4 10^{-5} kg m^{-2} s^{-1} : only 3% of the CO_2 condenses in the atmosphere in that case.

The presence of dust strongly increases the emissivity of the atmosphere, and thus the cooling rate. In our model, in which the dust mixing ratio is constant from the surface to an altitude of about 40 km (it is progressively reduced above 40 km), the radiative cooling rate is a maximum near the ground and slowly decreases with altitude. Because the atmospheric density also decreases with altitude, more than half of the carbon dioxide snow reaching the ground is formed in the first 5 km.

The radiative properties of the surface also affect the radiative equilibrium of the atmosphere. When the cap surface emissivity ε is lower than one (outside the CO_2 15 μm absorbtion band), as suggested by some observations (see Forget *et al.* 1995), the infrared "heating" of the atmosphere by the ground is reduced, and the condensation increases. When the atmosphere is dust laden or when water ice particles are present, this effect should be non negligible. This is illustrated by the case $\varepsilon = 0.7$ and $\tau = 1$ in Fig. 1. Reducing the emissivity by 30% leads to an increase of the cooling rate and the condensation rate by about the same order. In that case, the rate of condensation on the ground is only 2.6 10^{-5} kg m^{-2} s^{-1}. The fraction of CO_2 condensing in the atmosphere reaches 25%. However, this effect should not occur when the atmosphere is clear of dust or water ice. In that case, the atmosphere can only absorb in the CO_2 15 μm band, a spectral region where the CO_2 ice emissivity is, always close to one (even if its wavelength averaged emissivity is low).

3.2 Adiabatic cooling

Cooling by the atmospheric large scale circulation. The atmospheric circulation affects the thermal structure of the polar atmosphere in several ways. On the one hand, the atmosphere transports heat from the insolated latitudes to the polar regions (see Pollack *et al.* 1990, Hourdin *et al.* 1995). On the other hand, the circulation can locally adiabatically warm or cool the atmosphere. Cooling occurs in upward motions, for instance when the wind is directed upslope.

Both the heat advection and the large scale adiabatic effects can be simulated with the GCM. Let us consider results from a simulation of the southern winter performed with a clear atmosphere ($\tau = 0$). Fig. 2 shows the total atmospheric condensation rate (i.e. the amount of CO_2 ice formed in the atmosphere precipitating on the ground) at $L_s = 120^o$, averaged over 1 day. In two separate areas around 75^{o}S-135^{o}W and 67.5^{o}S-20^{o}W, the atmospheric condensation rate reaches more than ten times the value corresponding to the radiative cooling alone. According to Fig. 3, which shows the various components of the energy balance of the atmospheric column at 75^{o}S-135^{o}W, a strong dynamical adiabatic cooling related to the general circulation is added to the radiative cooling. This cooling is especially intense in the first six kilometers above the surface. The corresponding condensation rate and precipitation rate are shown in Fig. 4, along with the rates observed at 67.5^{o}S-20^{o}W. At this last location, the

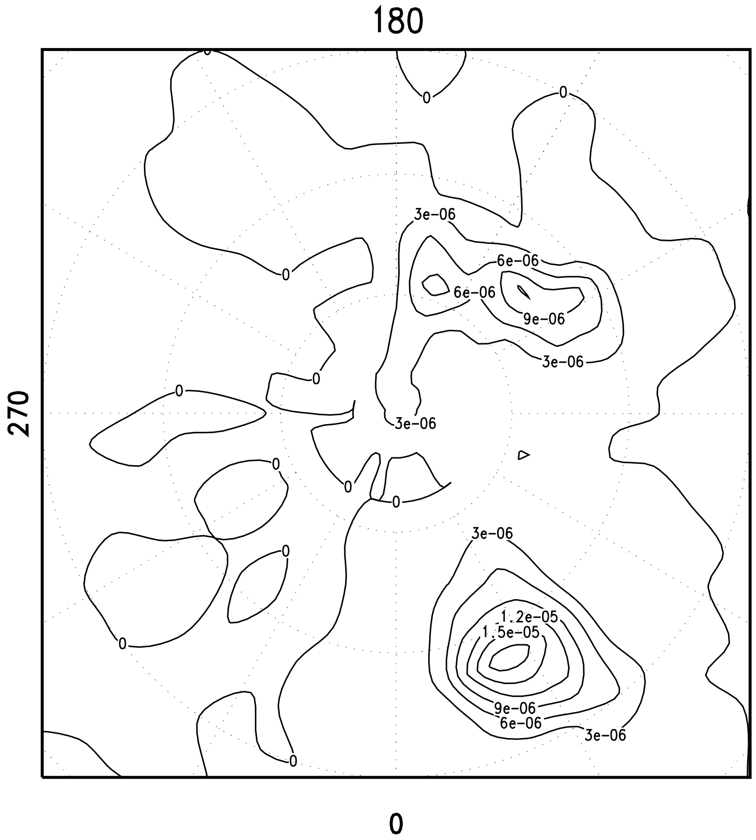

Figure 2: A typical map of the atmospheric condensation rate (kg m^{-2} s^{-1}) simulated by the GCM in the south polar region in winter (average over one day at $L_s = 120^o$) for a clear atmosphere ($\tau = 0$). Latitude circles are spaced by 10^o.

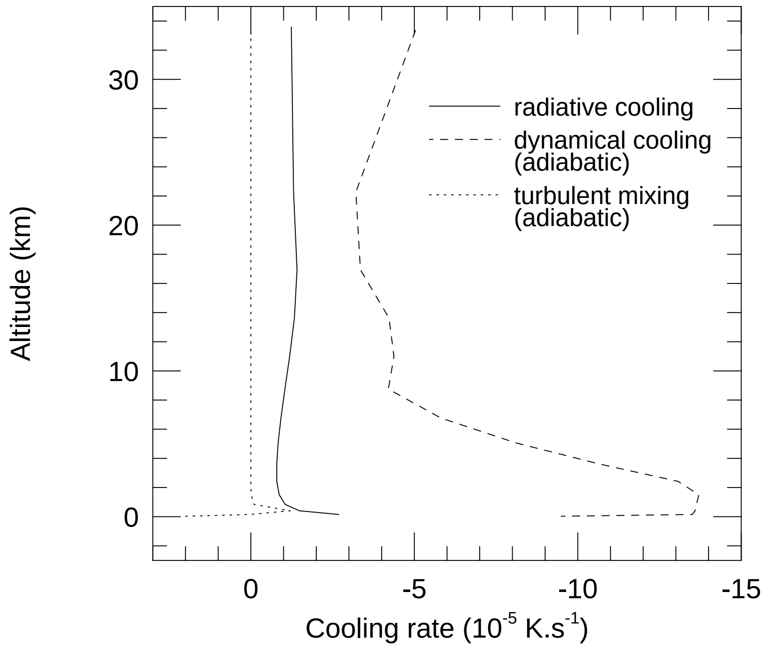

Figure 3: Analysis of the energy balance of the atmosphere at 75^{o}S-135^{o}W for the GCM run shown in Fig. 2, in a region where the atmospheric condensation rate is particularly intense.

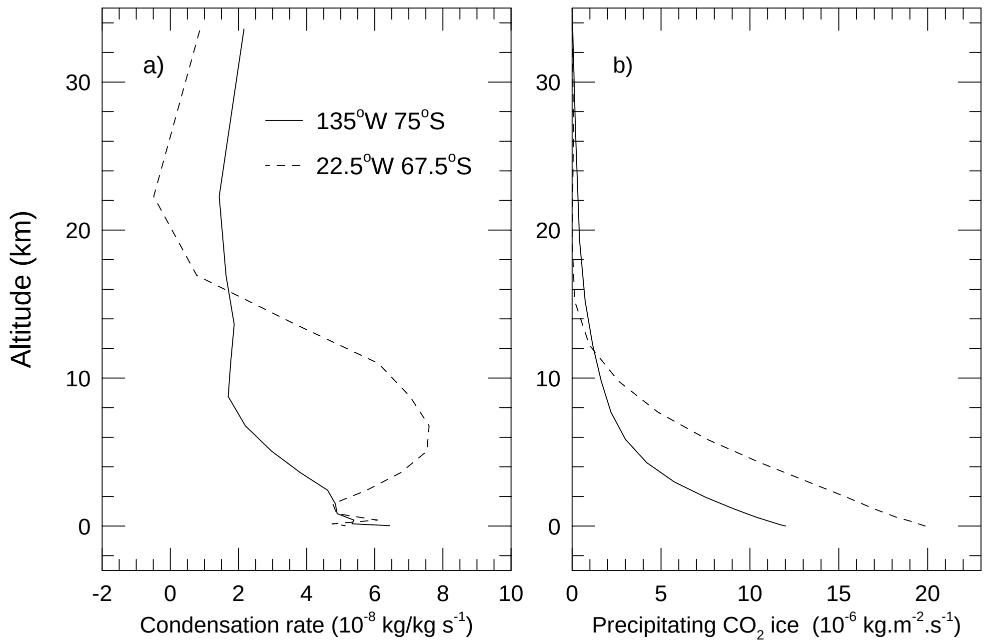

Figure 4: vertical profile of the condensation and integrated precipitation rate at 75^{o}S-135^{o}W and 67.5^{o}S-22.5^{o}W for the GCM run shown in Fig. 2.

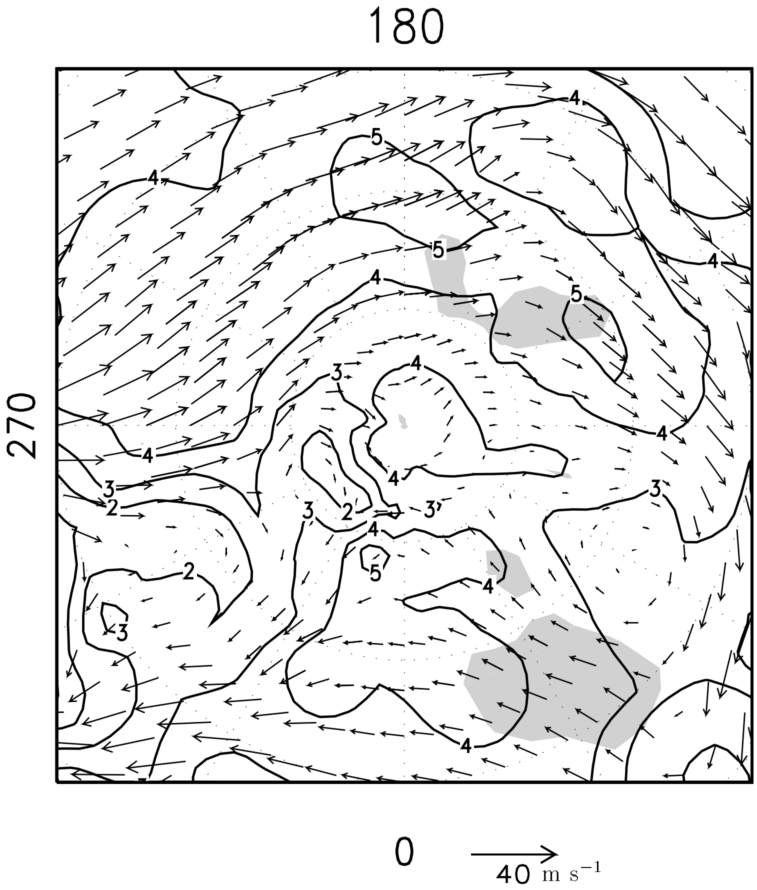

Figure 5: Wind vectors at 1 km above the surface for the GCM run shown in Fig. 2, superimposed on topography contours of the south polar region. Areas where the local atmospheric condensation rate is larger than 10^{-8} kg s^{-1} per kg of atmosphere are shaded. This map shows that condensation occurs in upward flows, due to adiabatic cooling. Latitude circles are spaced by 10^o.

condensation rate is negligible above 15 km, with a maximum near 6 km. In both cases, most of the snow reaching the ground is formed in the first 10 km above the surface.

By which dynamical mechanism are these two condensation zones created ? Fig. 5 illustrates the relationship between the atmospheric condensation and the general circulation. The wind field at about 1 km above the surface is structured around two low-pressure zones located at about 60^oW and 300^oW. This structure is typical of the southern winter stationary waves which are forced by the topography (Fig. 5 shows that both regions correspond to low altitude areas related to the Argyre and Hellas basins). One can see in Fig. 5 that atmospheric condensation occurs where the wind is directed upslope of high topography regions. There, winds of the order of $U = 10$ m s^{-1} blow up slopes of typically $x \simeq 0.3\%$. The vertical components of such winds is therefore $W \simeq xU \simeq 0.03$ m s^{-1}. Simple thermodynamic considerations show that the corresponding adiabatic cooling rate can be expressed as :

$$\frac{\partial T}{\partial t} = -W(\frac{g}{c_p} + \frac{\partial T}{\partial z}) \quad (1)$$

where g is the acceleration of gravity, c_p is the specific heat at constant pressure, and $\partial T/\partial z$ the local lapse rate. Assuming that the temperature profile follows the CO_2 condensation temperature ($\partial T/\partial z \simeq -1$ K km^{-1}) we obtain an adiabatic cooling rate of the order of 10^{-4} K s^{-1}, a value comparable with the results displayed in Fig. 3. If the wind blows downhill, the opposite effects occurs (Foehn wind effect). For instance, in the basin located near the pole at 300^{o}W, the atmosphere is warmed up to 3 K above the condensation temperature by adiabatic compression.

Cooling by the small-scale circulation. In reality, adiabatic cooling leading to atmospheric condensation may occur upon sub-grid scale topographic features which are not resolved by the GCM. Thus, in some places, the model probably underestimates the amount of CO_2 ice particles condensing in the atmosphere. However, once formed, these particles should be transported downstream, down the topographic feature. As for the terrestrial lenticular clouds, they are then likely to resublimate before growing enough to contribute to the mean "precipitation". Lee wave clouds are also likely to form, but again, they should not significantly affect the precipitation rate. Clouds formed by one of these topographic features alone should be optically very thin in the infrared since cloud particles should not grow enough to significantly affect the infrared radiation (a few μm at least are required ; see Forget *et al.* 1995).

Impact of the turbulent mixing in the boundary layer. The atmospheric boundary layer is the region near the surface where turbulence mixes heat, mass and momentum and induces some exchange between the ground and the atmosphere. Since the winter polar atmosphere is very stable, atmospheric turbulence can only be generated by mechanical instability (wind shears near the ground). This mixing is adiabatic. It tends to homogenize the potential temperature θ. Since the adiabatic temperature profile (constant θ) is much steeper than the condensation temperature profile (-5 K/km versus -1 K/km), heat exchange in the boundary layer results in a cooling of the upper part of the boundary layer and a warming of the lower part. This behavior is noticeable in Fig. 3. The dotted line shows the contribution of turbulence to the cooling rate at 75^{o}S-135^{o}W for the case previously studied. The turbulence is forced there by a 15 m s^{-1} wind at 1 km above a surface of roughness height $z_o = 1$ cm. Compared to the radiative and dynamical cooling rate, the impact of the turbulent mixing is small. Overall, warming and cooling tend to balance each other. The net effect of turbulent mixing is a very small increase in the total atmospheric condensation rate, due to the "cooling" (in terms of potential temperatures) of the atmosphere by the ground.

4 Modeling the radiative effect of CO_2 snow

4.1 The CO_2 snow scheme

As explained in the introduction, CO_2 ice particles that condense in the atmosphere can be efficient scatterers at infrared wavelengths, whether they are airborne (clouds with particle radius $> 10\mu$m) or have just fallen to the ground (fresh snow) (Forget *et al.* 1995). We have seen that the amount of CO_2 condensing in the atmosphere can be estimated with the GCM. Unfortunately, not much is known about the CO_2 clouds microphysics and even less about the processes which control the metamorphism of the CO_2 snow at the surface. Consequently, linking the CO_2 condensation rate with the actual radiative effect of the cloud and snow on the basis of physical considerations is not straightforward. Thus we make several assumptions. First, we have chosen not to distinguish between airborne snow flakes and surface snow. Indeed, the available observations do not permit us to distinguish between these two cases, and it is not known wether the reduction of the infrared fluxes emitted by the polar regions is primarily due to the snow in the air or on the ground. In fact, both surface snow (by reducing the surface emissivity) and clouds (by backscattering the infrared radiation) decrease the net infrared radiative fluxes at the surface and at the top of the atmosphere. For the ground, and for the atmosphere above the top of the scattering clouds, the radiative budget is the same in both cases. In the model, the radiative effects of CO_2 snow and clouds have therefore been parametrized by simply decreasing the surface emissivity ε. The main impact of such a simplification is to underestimate the upward and downward infared fluxes in the layers located between the surface and the top of the scattering cloud. When the atmosphere is clear, this should not affect the condensation rate, since the radiation is backscattered at wavelengths which, by definition, cannot be absorbed by the CO_2 ice and gas. When the atmosphere is dust laden, our assumption might lead to an overestimate of the atmospheric cooling rate, and in turn, of the atmospheric condensation. However, only the layers located below the scattering clouds with particle radii $> 10\mu$m (and thus close to the ground) should be affected.

The surface emissivity ε in our model is thus supposed to account for the variation of the actual emissivity of the system [ground + ice + fresh snow + clouds]. ε will decrease with the accumulation of particles having condensed in the atmosphere. During a snowfall at a given time, atmospheric condensation accumulates a layer of mass m (kg m^{-2}) of scattering particles. The particle sizes in this layer are probably extremely variable, from the top of the clouds to the snow layers underneath. For our parametrization, a detailed knowledge of the vertical distribution of the particle sizes is not required since we are only concerned with the global impact of the entire layer on the radiation budget. Thus, we can assume that the size distribution in this layer can be represented by a single effective radius r. This radius probably ranges between 10 μm (the minimum size to efficiently scatter thermal radiation) and a few hundreds micrometers, consistently with microphysical considerations (Wood *et al.* 1996).

At a given wavelength, the optical depth corresponding to mass m is given by:

$$\tau = \frac{3Q_{ext}}{4\rho r} m \tag{2}$$

Where ρ is the CO_2 ice density (about 1630 kg m^{-3} at 140 K) and Q_{ext} the extinction parameter. At 20 μm, where the CO_2 ice is almost transparent, Q_{ext} should be close to the scattering parameter Q_{scat}. For particles larger than 25 μm, Q_{ext} should therefore be close to the asymptotic value 2. For particles with radii between 10 and 25 μm, according to the Mie theory, Q_{ext} may theoretically reach 4 because of resonance processes. In reality, however, the broad size distribution should decrease these

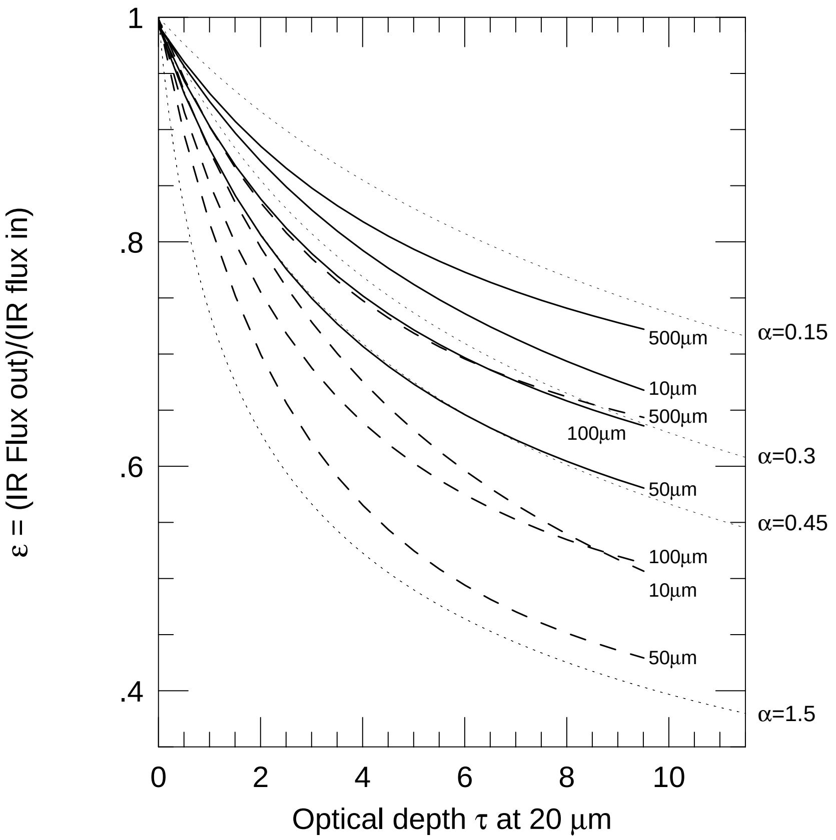

Figure 6: Reduction of the outgoing infrared flux due to a layer of CO_2 ice particles of radius 10, 50, 100 and 500 μm, and of various optical depths. The particles and surface temperature is 145 K. CO_2 ice is pure (dashed lines) or mixed with 10 g.m^{-2} of water ice (solid lines). Dotted lines show examples of the curve $\varepsilon = (1 + \alpha\tau)^{-1/3}$, used to fit the results of the radiative transfer model.

effects (Hansen and Travis 1974) and we can also take $Q_{ext} \simeq 2$. The optical depth τ should thus only be a function of r and m. In S.I. units, $\tau \simeq 10^{-3}\ m/r$.

The impact of such a layer of optical depth τ on the thermal radiation can be computed with a radiative transfer model. The model employed in our calculations is basically the same as that used by Forget *et al.* (1995) and described in more detail by Toon *et al.* (1989) and Pollack *et al.* (1993b). This algorithm is based on the two-stream, hemispheric mean, source function solution to the equation of radiative transfer and allows for the emission angle of the observations. The single-scattering calculation follows Mie theory. The results, presented in Fig. 6, show that at a given wavelength, the decrease of infrared flux due to backscattering depends upon the particle radius and the amount of water ice mixed with the CO_2 ice (such water ice particles are thought to be present at least in the northern hemisphere). The vertical axis in Fig. 6 corresponds to the emissivity ε of the system ground + scattering layer that we are parameterizing. In most realistic cases, ε is well approximated by $\varepsilon = (1 + \alpha\tau)^{-1/3}$ with $0.15 < \alpha <$

1.5, $\alpha = 0.45$ being an appropriate mean value. Using $\tau \simeq 10^{-3}\, m/r$ yields :

$$\varepsilon = (1 + 10^{-3}\, \frac{\alpha}{r} m)^{-1/3} \tag{3}$$

Differentiation with respect to time gives the equation governing the decrease of ε:

$$\frac{\partial \varepsilon}{\partial t} = -\frac{10^{-3}}{3}\, \varepsilon^4\, \frac{\alpha}{r} \frac{\partial m}{\partial t} \tag{4}$$

$\partial m/\partial t$ corresponds here to the atmospheric condensation rate (kg.m^{-2}.s^{-1}).

In reality, the decrease of ε due to the CO_2 snowfall is probably limited by the fact that, once on the ground, the CO_2 snow flakes progressively loose their scattering properties. Indeed, the continuing surface condensation should tend to aggregate the grains. A kind of "destructive metamorphism" may also play a role (Eluszkiewicz 1993). To simplify, we have assumed that ε was restored toward unity with a characteristic timescale $\mathcal{T}$. This timescale should be of the order of the low emission zones time scale observed by Viking, probably less than one day (Kieffer *et al.* 1977, Forget *et al.* 1995). In our model, the governing equation for the emissivity ε as a function of the condensation rate $\partial m/\partial t$ becomes :

$$\frac{\partial \varepsilon}{\partial t} = -\frac{10^{-3}}{3}\, \varepsilon^4\, \frac{\alpha}{r} \frac{\partial m}{\partial t} + \frac{1}{\mathcal{T}}(1 - \varepsilon) \tag{5}$$

This parametrization depends on only two "unknown" parameters, namely $\mathcal{T}$ and r (actually α/r, but α is set to its mean value $\alpha = 0.45$, r remaining variable). Moreover, the stationary solution of equation 5 (corresponding to $\partial\varepsilon/\partial t = 0$) only involves the ratio $r/\mathcal{T}$. On average, this ratio will control the value of ε, making the model very simple.

In practice, Equation 5 was implemented in the model by incrementing ε at each timestep ($\varepsilon_{t+\delta t} = \varepsilon_t + \delta\varepsilon$). To ensure numerical stability, $\delta\varepsilon$ was calculated using an analytical approximation of equation 5 integrated over one timestep :

$$\delta\varepsilon = [\varepsilon_t^{-3} + 10^{-3} \delta t\, \frac{\alpha}{r} (\frac{\partial m}{\partial t})_t]^{-1/3} - \varepsilon_t + \frac{\delta t}{\mathcal{T}}(1 - \varepsilon_t) \tag{6}$$

4.2 Simulation of the low emission zones

The model performance can be assessed by comparing the low emission zones simulated by the model with the ones actually observed by Viking (not enough data were obtained by Mariner 9 ; see Forget *et al.* 1995). The low brightness temperatures were observed by the IRTM instrument aboard Viking with its 20-μm channel: T_{20}. To simulate T_{20} from the model output, results from Forget *et al.* (1995)'s radiative transfer cloud and snow models were used. These models are able to simulate the spectra observed in the low emission zones. Because the condensing polar night atmosphere is almost isothermal in the first tens of kilometers where dust and water ice are usually expected, we assumed that T_{20} was unaffected by the absorption and emission of these aerosols during the studied periods (i.e. outside the peak of dust storm b between $L_s = 273^o$ and $L_s = 290^o$).

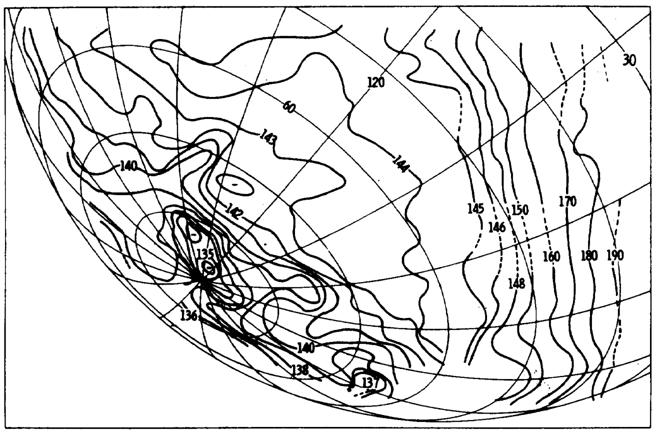

(a) T_{20} observed by Viking (K)

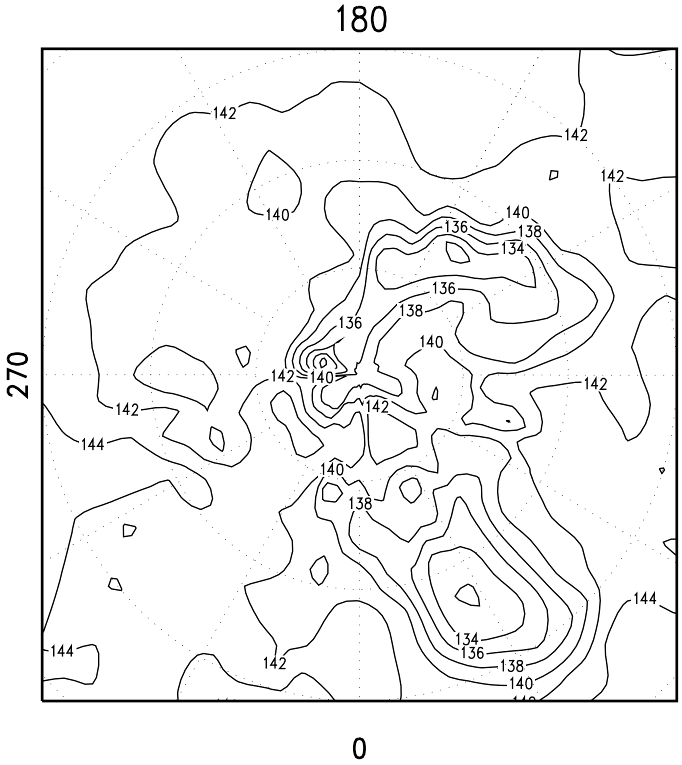

(b) T_{20} simulated by the model (K)

Figure 7: Examples of spatial patterns of the 20-μm brightness temperatures T_{20} (a) observed by the Viking IRTM instrument during the winter in the south polar region ($L_s = 93^o$, figure from Kieffer *et al.* 1976), and (b) simulated by the model ($\tau = 0.1$, $L_s = 120^o$).

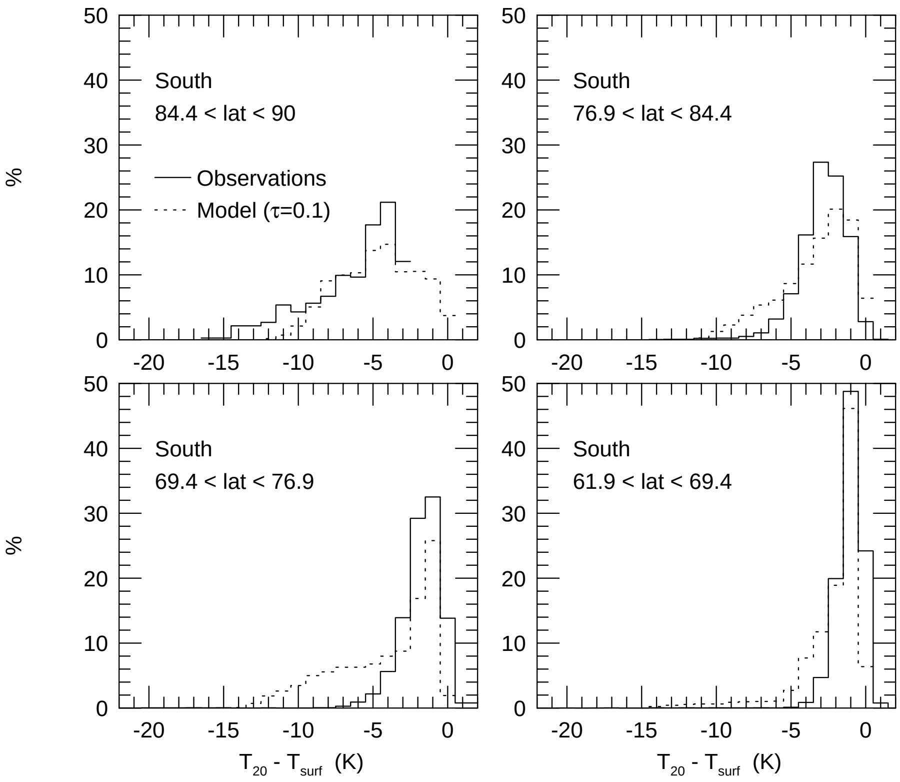

Figure 8: Comparisons of the low emission zones distribution observed by Viking in the southern hemisphere during $L_s = 90 - 120^o$ and simulated by the GCM (from a 15-day run corresponding to $L_s = 112 - 119^o$). The intensities of the low emission zones are quantified by the difference between the brightness temperature T_{20} and the cap surface temperature. tn each latitude belt, The histograms show the percentage of observations or model output obtained with $T_{20} - T_{\text{surf}}$ in the same 1 K bin (e.g. $-5.5 < T_{20} - T_{\text{surf}} < -4.5\ K$) during the studied period. In the model, the mean CO_2 snow particle radius r is 100μm and the snow metamorphism timescale $\mathcal{T}$ is 0.5 days The dust optical depth τ is set to 0.1.

T_{20} could thus be computed only from the modeled surface temperature T_{surf} and cap emissivity. In practice, we simplified the calculation by using a linear approximation :

$$T_{20} = T_{\mathrm{surf}} - 43(1 - \varepsilon) \tag{7}$$

with T in Kelvins. This proved to be a fairly good approximation in most realistic cases and for moderate viewing angles ($< 60^o$). Fig. 7b shows an example of T_{20} temperature fields simulated by the GCM during southern winter. For this simulation, the mean CO_2 snow particle radius r was set to 100μm as expected from physical considerations, and the metamorphism timescale $\mathcal{T}$ was fixed to 0.5 day in accordance with the typical time scale of the low emission zones. No particular tuning was done. Yet, the spatial scale and intensity of the low emission zones are very close to the actual measurements (compare with Fig. 7a which shows an example of the spatial patterns of T_{20} measured by the IRTM instrument).

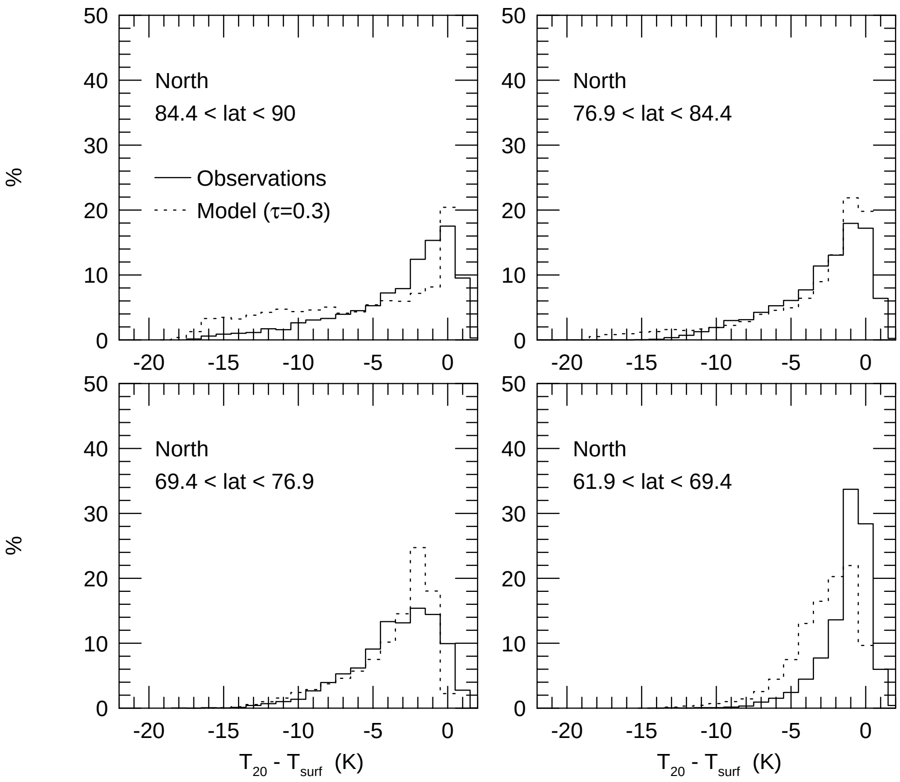

Figure 9: Same as Fig. 8 but for the northern hemisphere with IRTM observations obtained before the second Viking global dust storm ($L_s = 240^o - 270^o$) and a 15-day GCM simulations ($L_s = 263^o - 273^o$) with $\tau = 0.3$.

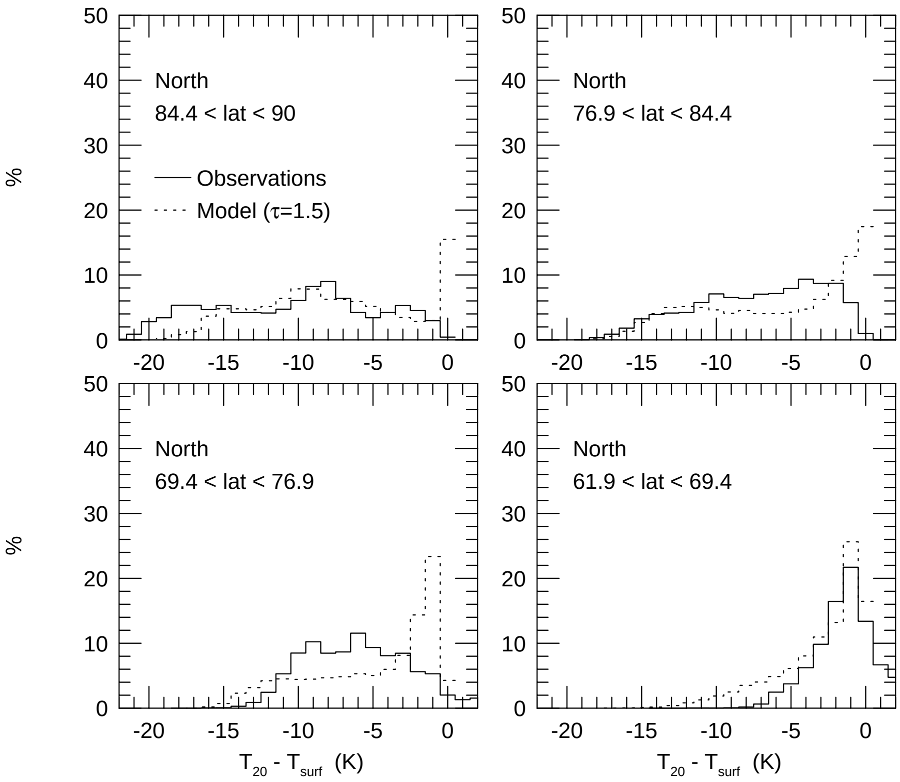

Figure 10: Same as Fig. 9 with IRTM observations obtained after the second Viking global dust storm ($L_s = 290^o - 310^o$) and a 15-day GCM simulations ($L_s = 263^o - 273^o$) with $\tau = 1.5$.

In both hemispheres, a detailed comparison of the simulated and observed spatial patterns is made difficult by the limited coverage of the data on the one hand, and by the fact that atmospheric condensation strongly depends on the poorly known topography, on the other hand. Nevertheless, we have been able to compare the model results with the observations quantitatively by looking at the statistical distribution of the low emission zones, identified by the difference between T_{20} and the cap surface temperatures (as retrieved by Forget and Pollack (1996) from the observations). Comparisons in four latitudinal belts in each hemisphere are presented in Figs. 8, 9 and 10. Again, the CO_2 snow scheme parameters were not tuned ($r = 100\mu$m, $\mathcal{T} = 0.5$ day). However, we used different values of the atmospheric dust optical depth τ, a key parameter with regard to atmospheric condensation, but which is poorly known in the polar regions. We found that, with these particular snow parameters, the low emission zone distributions were well simulated with $\tau = 0.1$ in the southern hemisphere (Fig. 8). In the northern hemisphere, the observed distribution of the low emission zones strongly varied with time probably because of the fluctuations of the dust cycle. Such variations can be reproduced by the model. For instance, the distribution observed during the relatively clear period preceding the second global dust storm observed by Viking ($L_s = 240^o - 270^o$) can be well reproduced with $\tau = 0.3$ (Fig. 9), whereas the numerous low emission zones observed after the storm around $L_s = 290^o - 310^o$ can be simulated with $\tau = 1.5$ (Fig. 10).

These dust optical depths are slightly lower than the ones observed by the Viking Landers at the same period (Colburn *et al.* 1989), but their relative values are very realistic. In fact, Mariner 9 limb observations (Anderson and Leovy 1978) and dust storms 3D model results (Murphy *et al.* 1995) do suggest that the dust optical depths in the winter polar region should be lower than those recorded by the Viking Landers. In any case, these results suggest that the CO_2 snow scheme is physically plausible. In our opinion, this supports the CO_2 snow fall scenario suggested by Forget *et al.* (1995).

5 A realistic simulation of the global CO_2 cycle

As explained in the introduction, several models have been used in the past to simulate the Martian seasonal CO_2 cycle, and in particular the seasonal evolution of the atmospheric mass responsible for the large pressure oscillations observed by the Viking Landers. Most recent models have been able to reproduce the general forms of the cap seasonal evolution including the Viking Landers pressure variations (e.g., Wood and Paige 1992, Pollack *et al.* 1993a, Hourdin *et al.* 1993, 1995) . However, these studies found that the amount of CO_2 actually condensing in the polar cap was about 30% lower than predicted if the caps were assumed to be blackbody emitters. To fit the Viking pressure data, they thus used low values (e.g., 0.7) for the modeled cap emissivities in spite of the fact that such values are likely to be artificial. Indeed, the caps emissivity seems to be near unity at least during the early fall and late winter seasons (Paige 1985), and more generally outside the low emission zones (Forget *et al.* 1995).

Recently, Forget and Pollack (1996) carefully reanalyzed the Viking infrared thermal mapper (IRTM) measurements and suggested that the models' tendency to overestimate the CO_2 condensation rate could be explained by a combination of causes, including the radiative effects of the low emission zones, as well as the overestimation of the polar cap surface temperatures in the models, and the underestimation of the heat advected to the polar cap region during the dusty seasons. In this section, we show that a model using a physically based parametrization of the low emission zones, exhibiting realistic cap surface temperatures and allowing for the seasonal variations of the atmospheric dust content can indeed reproduce the Martian seasonal pressure cycle without using artificially low ice emissivities.

Tuning of the polar cap surface temperatures. Because the polar caps are in solid-gas equilibrium with the atmosphere, the cap surface temperature simply depends on the surface pressure, and, in turn, on the topography. However, the large-scale Martian topography is still poorly known, and two rather different data sets have been used by modelers: The "Mars Consortium" and the "Digital Terrain Map" (DTM, officially called Digital Elevation Model, or DEM). Fig. 11 shows the zonal averaged frost point temperatures computed by the GCM with both datasets at winter solstice compared to the surface temperatures derived from the IRTM observations by Forget and Pollack (1996). In all of the simulations, the atmospheric mass was adjusted to match the surface pressure observed at the Viking Lander 1 site. Until recently, most GCMs, and in particular the LMD GCM, had used the Consortium topography dataset. With this dataset, in the southern hemisphere, the modeled frost point of CO_2 appears to be much warmer than the surface temperatures retrieved from the IRTM data. The discrepancy is reduced when using the DTM dataset, although DTM is still 2-3 K warmer than the observed temperatures in both hemisphere. To account for this discrepancy, we have set the maximum cap surface emissivity to 0.95, as for the rocky surface elsewhere on the planet. In terms of radiative fluxes, the agreement is then much better in both polar regions, as shown in Fig. 11.

Taking into account the seasonal dust cycle. In order to reproduce the observed low emission zones hemispheric asymmetry and to treat the advection of heat by the atmosphere properly, it was necessary to take into account the dust seasonal variations. A baseline scenario was built by varying the global dust optical depth τ as a function of season with $\tau = 1. + 0.5\cos(L_s + 80^o)$. Such a function is thought to roughly reproduce the observed variations at the Viking Lander 1 site during the second and the third Viking year (Pollack *et al.* 1993a). The corresponding low emission zone distributions, although not as close to the observations as in Figs. 8, 9 and 10, remain realistic in both hemispheres.

The first Viking year was quite different from this baseline scenario with two global dust storms occuring during the early northern fall and early northern winter. To study the impact of such dust storms on the modeled CO_2 cycle, we added two optical depth peaks to the sinusoidal function of the baseline scenario in order to roughly match the seasonal variation of the dust opacity measured at Viking Lander 1 during Viking year 1 (Fig. 12a).

In both the baseline and dust storms scenarios, the enhanced dust loadings during northern winter increase the atmospheric heat transport into the polar cap regions (Pollack *et al.* 1990, Hourdin et al. 1995). In particular, the use of a new version of the GCM with a top above 80 km allows for the simulation of the adiabatic warming

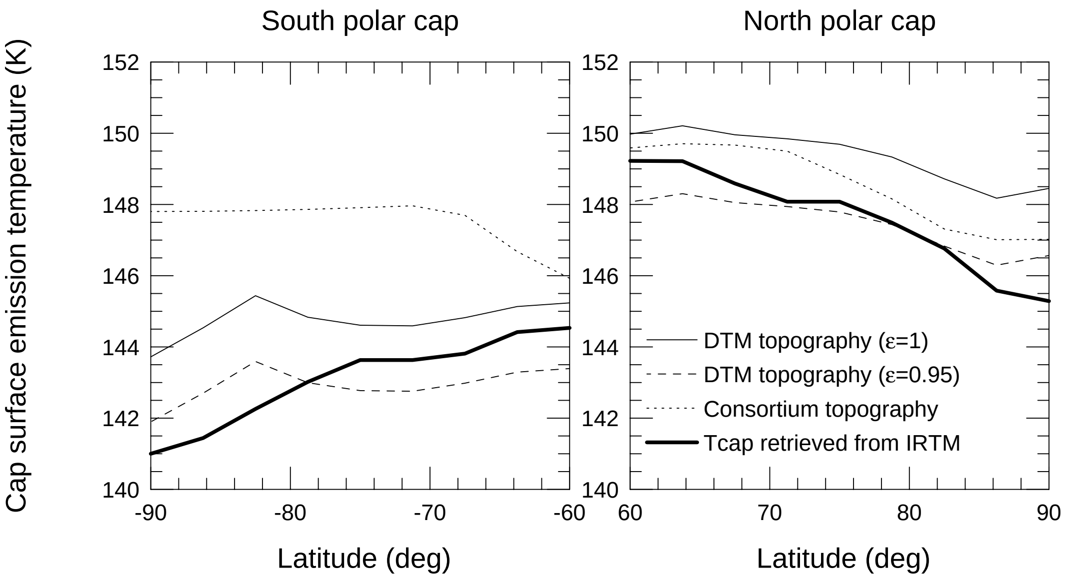

Figure 11: Comparison of zonally-averaged surface temperatures calculated by the GCM using the DTM and Consortium topography data sets with the surface temperatures retrieved from the IRTM data by Forget and Pollack (1996) (the temperature shown for $\varepsilon = 0.95$ is an equivalent temperature, in terms of radiative fluxes).

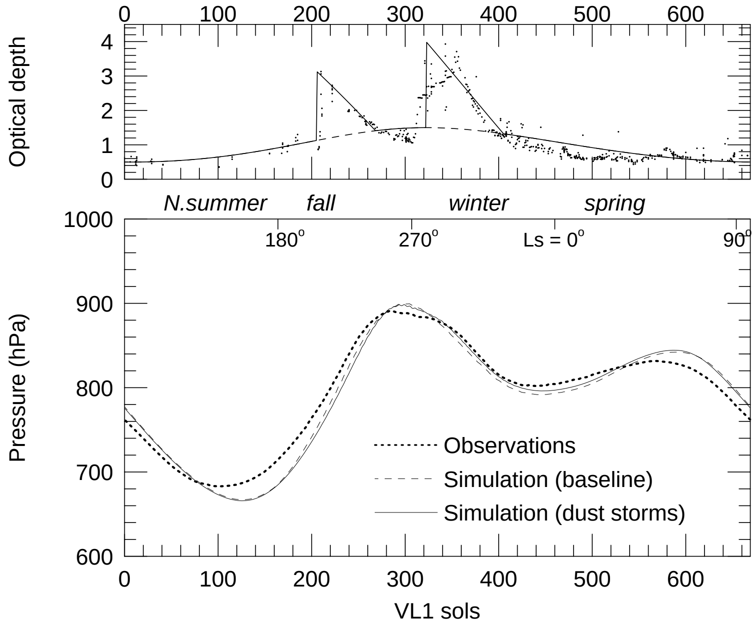

Figure 12: (a) Variation of the dust optical depth in the baseline scenario (dashed curve) and the dust storm scenario (solid curve) compared to the atmospheric opacity observed by the Viking Lander 1 during the first year of the mission (dots). (b) Pressures at the Viking Lander 1 site observed during the first year of the mission and simulated by the model. The pressures variations are smoothed using a 30 days running average to remove the signature of the thermal tides and baroclinic waves. The model was run with our new CO_2 snow fall parametrisation ($r = 100\mu$m, $\mathcal{T} = 0.5$ day), a constant cap albedo of 0.5, DTM topography, and the varying dust optical depths as shown above.

of the upper northern atmosphere ("polar warming" ; See Wilson 1997, Forget *et al.* 1996). This warming is a non-negligible component of the radiative budget of the polar regions especially during the dust storms (Forget and Pollack. 1996). It had not been taken into account in previous studies since, until recently, Martian GCMs were unable to simulate this phenomenon.

Viking Lander pressure To reproduce the annual pressure cycle observed by the Viking Landers, we have tuned the cap albedo and the total mass of the cap + atmosphere system using the procedure described in Hourdin *et al.* (1995). The snow emissivity scheme parameters r and $\mathcal{T}$ were kept to their "physical" values 100 μm and 0.5 day. We found that a reasonable fit to the Viking Lander 1 pressure measurements could be obtained in the baseline scenario by simply choosing a constant cap albedo equal to 0.5 in both hemispheres (Fig. 12). Such a value is consistent with the observations (See Table 4, Pollack *et al.* 1993a) and previous modelling studies (Wood and Paige 1992, Pollack *et al.* 1993a, Hourdin *et al.* 1995). A comparison with the Viking Lander 2 pressure measurements is not possible because the DTM topography used for this study puts Viking Lander 2 about 2 km too high with reference to the Viking Lander 1.

An additional run was performed for the dust storms scenario with the same atmospheric mass and cap properties. The impact of the modeled dust storms is relatively small, with in particular an increase of the surface pressure up to 6 hPa during northern winter and spring mostly due to the second viking dust-storm (the impact of the first dust storm on the modeled CO_2 cycle was found to be negligible). A part of this increase is due to the dynamical effect (see Hourdin *et al.* 1993) and to a 20% reduction of the total condensation rate during the peak of the dust storm. Such results, obtained with a model accounting for the first time for processes like CO_2 snow fall and polar warming, tend to confirm that the small interannual pressure variability observed by the Viking landers may be due to the weak sensitivity of the system to the peak of opacity during dust storms compared to the seasonal cycle of the background dust (Forget and Pollack 1996). However, these results must be regarded with some caution, since the spatial distribution of the dust is probably far from reality in the model. In particular, the model does not simulate the apparent disparition of the low emission zones during the peak of the dust storm (Forget and Pollack 1996).

Overall, we believe that theses simulation are a good step toward a complete understanding of the Martian CO_2 cycle. However, much could still be done to improve the simulation of the subliming phase of the polar caps. Although the recession of the polar cap boundaries is well represented in our model (the results are somewhat similar to the ones obtained with a previous version of the GCM by Hourdin *et al.* 1995, Fig.19), it is known that the polar cap albedo stongly varies with space and time (James 1979, Kieffer 1979, Ono and Paige 1995). In particular, these variations probably lead to the preservation of a permanent CO_2 deposit all year long near the south pole (Paige and Ingersoll 1985). This is not the case in our simulation. The modeled south polar cap completely sublimes by the beginning of summer.

APPENDIX: CO_2 condensation-sublimation numerical scheme

Condensation and sublimation in the atmosphere. The model atmosphere consist of N layers. In each layer, at each computational timestep, the CO_2 gas condenses when the temperature T^* predicted from the dynamical and radiative cooling rates is below the condensation temperature Tc. The temperature T is then set to Tc. The corresponding enthalpy deficit must be balanced by the CO_2 condensation. Condensation is computed from top to bottom. In the upper level N of the model, this yields :

$$\delta m_N = \frac{c_p M_N}{L}(Tc_N - T^*_N) \qquad (8)$$

With δm_N the mass of ice that has condensed (>0 when condensing), M_N the layer mass, c_p the specific heat at constant pressure (735.9 J kg^{-1} K^{-1} on Mars) and L the latent heat of CO_2 (5.9 10^5 J kg^{-1}). Below this level, the fact that the atmosphere might have condensed in the layers above must be taken into account :

$$\delta m_l = \frac{c_p M_l}{L}(Tc_l - T^*_l) - \frac{1}{L}[g(z_{l+1} - z_l) + c_{ice}(Tc_{l+1} - Tc_l)] \sum_{k=l+1}^{N} \delta m_k \qquad (9)$$

with z_l the altitude in the middle of layer l ; g the acceleration of gravity ; c_{ice} the specific heat of CO_2 ice (349+4.8T J kg^{-1} K^{-1}, with 73 K< T < 200 K, from

Washburn 1948); and $\sum_{k=l+1}^{N} \delta m_k$ the amount of ice that condensed in the layers above, falling from layer $l+1$. The term $[g(z_{l+1}-z_l)\sum_{k=l+1}^{N} \delta m_k]$ corresponds to the potential energy released by this amount of ice falling from layer $l+1$ (aerodynamical friction). The term $[c_{ice}(Tc_{l+1}-Tc_l)\sum_{k=l+1}^{N} \delta m_k]$ corresponds to the energy used to heat the mass $\sum_{k=l+1}^{N} \delta m_k$ from the temperature Tc_{l+1} to Tc_l. These two terms are not negligible: 1 kg of ice condensed at $z = 10$ km (about one atmospheric scale height) would release $gz = 3.73\ 10^4$ J and would consume $c_{ice}(Tc(z) - Tc(0)) \simeq -10^4$ J, respectively 6.3 and 1.7% of the latent heat initially released (5.9 10^5 J).

The ice condensed in the atmosphere can resublime during its descent if it encounters warm layer with $T_l > Tc_l$. Equation 9 then remains valid and the amount $\delta m_l < 0$ is sublimed. However, if all the ice falling from the layers above sublimes in layer l (case when equation 9 predicts: $-\delta m_l > \sum_{k=l+1}^{N} \delta m_k$), we set $\delta m_l = -\sum_{k=l+1}^{N} \delta m_k$ and the layer temperature T_l is then given by:

$$T_l = T_l^* + \frac{1}{c_p M_l}[-L + g(z_{l+1} - z_l) + c_{ice}(Tc_{l+1} - Tc_l)] \sum_{k=l+1}^{N} \delta m_k \qquad (10)$$

Condensation and sublimation on the ground. Condensation on the ground is controlled by the same kind of equation as for atmospheric condensation. Equation 9 remains valid with $l = 0$ and replacing $c_p M_l$ by $c_s A$, with A the area of the grid mesh and c_s the surface heat capacity (in J m^{-2} K^{-1}). At each timestep, in the model, the mass $\sum_{k=0}^{N} \delta m_k$ is added to the amount of ice on the ground m_0. We set $T_0 = Tc_0$, unless the ground ice completly sublimes (case when $-\delta m_0 > m_0 + \sum_{k=1}^{N} \delta m_k$ is predicted). We then set $\delta m_0 = -m_0 - \sum_{k=1}^{N} \delta m_k$ and the new surface temperature is expressed as:

$$T_0 = T_0^* - \frac{L}{C_s A} m_0 - \frac{1}{C_s A}[L - gz_1 - c_{ice}(Tc_1 - Tc_0)] \sum_{k=1}^{N} \delta m_k \qquad (11)$$

Energy and mass balance in vertical coordinates σ=p/p_0. The loss of atmospheric mass due to condensation (or conversely the gain due to sublimation) is taken into account by modifying the surface pressure at each timestep by :

$$\delta p_0 = -\frac{g}{A} \sum_{k=0}^{N} \delta m_k \qquad (12)$$

This ensures the conservation of the total mass of CO_2 (caps + atmosphere). However, in each layer, the condensation-sublimation induces some transfers of mass, heat and momentum which require a specific treatment. In particular, like in most GCMs, the layers in our model are defined by fixed coordinates $\sigma = p/p_0$. The changes in p_0 due to the CO_2 condensation-sublimation induce "artificial" movements of the σ levels in the atmosphere. This must be reflected in the temperature and wind fields. In a grid mesh of area A, let's consider a layer l delimited by the levels $\sigma_{l-\frac{1}{2}}$ and $\sigma_{l+\frac{1}{2}}$. At each timestep, its mass $M_l = \frac{A}{g}(\sigma_{l-\frac{1}{2}} - \sigma_{l+\frac{1}{2}})p_0$ varies because of the global variation of p_0. Such a variation is associated with transfers of mass between the layers (on which one must add the sink corresponding to the local condensation $-\delta m_l$). The local mass balance may be written :

$$\delta M_l = \frac{A}{g}(\sigma_{l-\frac{1}{2}} - \sigma_{l+\frac{1}{2}})\delta p_0 = W_{l-\frac{1}{2}} - W_{l+\frac{1}{2}} - \delta m_l \qquad (13)$$

where $W_{l-\frac{1}{2}}$ is the air mass (kg) "transfered" through the level $\sigma_{l-\frac{1}{2}}$ (> 0 when up) during the timestep. Equations 12 and 13 may be combined to yield a recursive formula on W :

$$W_{l+\frac{1}{2}} = W_{l-\frac{1}{2}} - \delta m_l + (\sigma_{l-\frac{1}{2}} - \sigma_{l+\frac{1}{2}}) \sum_{k=0}^{N} \delta m_k \qquad (14)$$

with:

$$W_{\frac{1}{2}} = -\delta m_0 \qquad (15)$$

The knowledge of W can then be used to compute the exchange of heat and momentum between the layers. For c_pT (enthalpy), the local heat balance can be written :

$$\delta(M_l T_l) = W_{l-\frac{1}{2}}\overline{T}_{l-\frac{1}{2}} - W_{l+\frac{1}{2}}\overline{T}_{l+\frac{1}{2}} - \delta m_l \, Tc_l \qquad (16)$$

with $\overline{T}_{l-\frac{1}{2}}$ the mean temperature of the gas transported through the $\sigma_{l-\frac{1}{2}}$ interface. Various operators have been suggested in the litterature to calculate $\overline{T}_{l-\frac{1}{2}}$. Indeed, this process is similar to a classical transport process. A simple arithmetic average ($\overline{T}_{l-\frac{1}{2}} = (T_l + T_{l-1})/2$) could have been used for instance, but we found that, because of the thiness of the layers near the surface in our model, more accurate results were obtained with a higher order scheme. We used the "Van-Leer I" finite volume transport scheme (Van-Leer 1977, Hourdin and Armengaud 1997), with, on the ground, $\overline{T}_{\frac{1}{2}} = T_0$.

Separately, one can also write :

$$\delta(M_l T_l) \simeq M_l \delta T_l + T_l \delta M_l \qquad (17)$$

with δT_l a correction to be applied at every timestep in each layer after the CO_2 condensation or sublimation. Eqs 16 and 17 may be combined to obtain δT_l

$$\delta T_l = \frac{1}{M_l}[W_{l-\frac{1}{2}}(\overline{T}_{l-\frac{1}{2}} - T_l) - W_{l+\frac{1}{2}}(\overline{T}_{l+\frac{1}{2}} - T_l) + \delta m_l(Tc_l - T_l)] \qquad (18)$$

The first two terms, with $W_{l-\frac{1}{2}}$ and $W_{l+\frac{1}{2}}$, correspond to the re-arrangement of the temperatures over the entire column due to the pressure variations in σ coordinates. The last term $\delta m_l(Tc_l - T_l)$ is usually equal to zero when CO_2 condenses or partially sublimes since we then have $Tc_l = T_l$. However, when the CO_2 totally sublimes (case of the equation 10), it becomes a cooling term accounting for the mixing of the newly sublimed mass $-\delta m_l$ with the rest of the layer at $T_l > Tc_l$.

In the lower layer, equation 18 can be rewritten:

$$\delta T_1 = \frac{1}{M_1}[-\delta m_0(T_0 - T_1) - W_{1+\frac{1}{2}}(\overline{T}_{1+\frac{1}{2}} - T_1) + \delta m_1(Tc_1 - T_1)] \qquad (19)$$

The term $\delta m_0(T_0 - T_1)$ corresponds to the condensation-sublimation flux from the ground. This term can be considerable during the sublimation phase in spring and summer, when the temperature difference between the lower atmosphere and the ground reaches 50 K. The cooling of the first layer by the newly sublimed CO_2 is then comparable to a loss of energy $c_p(T_0 - T_1)/L \simeq 6\%$ of the latent heat initially required.

Similarly, the momentum distribution must be re-arranged, although condensation and sublimation cannot be considered as sinks or sources of momentum. For a wind component v, we shall simply write:

$$\delta v_l = \frac{1}{M_l}[W_{l-\frac{1}{2}}(\overline{v}_{l-\frac{1}{2}} - v_l) - W_{l+\frac{1}{2}}(\overline{v}_{l+\frac{1}{2}} - v_l)] \tag{20}$$

with, on the ground, $\overline{v}_{\frac{1}{2}} = v_1 \delta m_0 / M_1$ if $\delta m_0 > 0$ and $\overline{v}_{\frac{1}{2}} = 0$ if $\delta m_0 < 0$ (the velocity of the CO_2 gas that has just sublimed is zero).

Acknowledgement

We are grateful to Bob Haberle and Richard Fournier for their help and suggestions. Further thanks are extended to Christophe Hourdin Peter Read, Mat Collins, Steve Lewis and Jean-Paul Huot. This work was supported by the European Space Agency through ESTEC TRP contract 11369/95/NL/JG.

Bibliography

Anderson, E., and C. Leovy 1978. Mariner 9 television limb observations of dust and ice hazes on Mars. *J. Atmos. Sci.* **35**, 723–734.

Clancy, R. T., S. W. Lee, G. R. Gladstone, W. W. McMillan, and T. Rousch 1995. A new model for Mars atmospheric dust based upon analysis of ultraviolet through infrared observations from Mariner 9, Viking, and Phobos. *J. Geophys. Res.*, **100**, 5251–5263.

Colburn, D. S., J. B. Pollack, and R. M. Haberle 1989. Diurnal variations in optical depth at Mars. *Icarus* **79**, 159–189.

Eluszkiewicz, J. 1993. On the microphysical state of the martian seasonal caps. *Icarus* **103**, 43–48.

Forget, F., and J.B. Pollack 1996. Thermal infrared observations of the condensing martian polar caps: CO_2 ice temperatures and radiative budget. *J. Geophys. Res.* **101**, 16,865–16,880.

Forget, F., J. B. Pollack, and G. B. Hansen 1995. Low brightness temperatures of martian polar caps : CO_2 clouds or low surface emissivity? *J. Geophys. Res.* **100**, 21,119–21,234.

Forget, F., F. Hourdin, and O. Talagrand 1996. Simulation of the martian atmospheric polar warming with the LMD general circulation model, *Annales Geophysicae* **14**, C797.

Gierasch, P. J., and R. M. Goody 1968. A study of the thermal and dynamical structure of the martian lower atmosphere. *Planet. Space Sci.* **16**, 615–646.

Hansen, J. E., and L. D. Travis 1974. Light scaterring in planetary atmosphere. *Space Sci. Rev.* **16**, 527–610.

Hourdin, F. 1992. A new representation of the CO_2 15μm band for a martian general circulation model. *J. Geophys. Res.* **97**, 18,319–18,335.

Hourdin, F., P. Le Van, F. Forget, and O. Talagrand 1993. Meteorological variability and the annual surface pressure cycle on Mars. *J. Atmos. Sci.* **50**, 3625–3640.

Hourdin, F., F. Forget, and O. Talagrand 1995. The sensitivity of the martian surface pressure to various parameters: A comparison between numerical simulations and Viking observations. *J. Geophys. Res.* **100**, 5501–5523.

Hourdin , F. and Armengaud , A. 1997. Test of a hierarchy of finite-volume schemes for transport of trace species in an atmospheric general circulation model. Submitted to *Monthly Wheather Review*.

Hunt, G. E. 1980. On the infrared radiative properties of CO2 ice clouds: Applications to Mars. *Geophys. Res. Lett.* **7**, 481–484.

James, P. B., and G. R. North 1982. The seasonal CO_2 cycle on Mars : An application of an energy balance climate model. *J. Geophys. Res.* **87**, 10271–10283.

James, P. B., G. Briggs, J. Barnes, and A. Spruck 1979. Seasonal recession of Mars' south polar cap as seen by Viking. *J. Geophys. Res.* **84**, 2889–2922.

Kieffer, H. H., S. C. Chase, E. D. Miner, F. D. Palluconi, G. Münch, G. Neugebauer, and T. Z. Martin 1976. Infrared thermal mapping of the martian surface and atmosphere: First results. *Science* **193**, 780–786.

Kieffer, H. H., T. Z. Martin, R. Peterfreund, B. M. Jakosky, E. D. Miner, and F. D. Palluconi 1977. Thermal and albedo mapping during the Viking primary mission. *J. Geophys. Res.* **82**, 4249–4291.

Kieffer, H. H. 1979. Mars south polar spring and summer temperatures: a residual co_2 frost. *J. Geophys. Res.* **84**, 8263–8288.

Leighton, R. R., and B. C. Murray 1966. Behavior of carbon dioxide and other volatiles on Mars. *Science* **153**, 136–144.

Martin, T. Z. 1986. Thermal infrared opacity of the Mars atmosphere, *Icarus* **66**, 2–21.

Mellor, G. L., and T. Yamada 1974. A hierarchy of turbulence closure models for planetary boundary layers. *J. Atmos. Sci.* **31**, 1791–1806.

Murphy, J., J. B. Pollack, R. M. Haberle, C. B. Leovy, O. B. Toon, and J. Schaeffer 1995. Three dimensional numerical simulation of martian global dust storms. *J. Geophys. Res.* **100**, 26357–26376.

Ockert-Bell, M. E., J. F. Bell III, C. McKay, J. Pollack, and F. Forget 1997. Absorption and scattering properties of the martian dust in the solar wavelengths. *J. Geophys. Res.* **102**, 9039–9050.

Ono, A. M., and D. A. Paige 1996. IRTM observations of martian south polar frosts. *Bull. Am. Astron. Soc.* **28**, 1060.

Paige, D. A., and A. P. Ingersoll 1985. Annual heat balance of martian polar caps: Viking observations. *Science* **228**, 1160–1168.

Paige, D. A., and K. D. Keegan 1994. Thermal and albedo mapping of the polar regions of Mars : 2. south polar region. *J. Geophys. Res.* **99**, 25993–26013.

Paige, D. A., D. Crisp, and M. L. Santee 1990. It snows on mars. *Bull. Am. Astron. Soc.* **22**, 1075.

Paige, D. A., J. E. Bachman, and K. D. Keegan 1994. Thermal and albedo mapping of the polar regions of Mars using viking thermal mapper observations 1. North polar region. *J. Geophys. Res.* **99**, 25959–25991.

Paige, D. A. 1985. *The annual heat balance of the martian polar caps from Viking observations*. Ph.D. thesis, Calif. Inst. of Technol., Pasadena.

Palluconi, F. D., and H. H. Kieffer 1981. Thermal inertia mapping of Mars from 60^oS to 60^oN. *Icarus* **45**, 415–426.

Pierrehumbert, R. T., and C. Erlick 1997. On the scattering-greenhouse effect of CO_2 ice clouds. *J. Atmos. Sci.*, in press.

Pleskot, L. K., and E. D. Miner 1982. Time variability of martian bolometric albedo. *Icarus* **50**, 259–287.

Pollack, J. B., C. B. Leovy, P. W. Greiman, and Y. Mintz 1981. A martian General Circulation Model experiment with large topography. *J. Atmos. Sci.* **38**, 3–29.

Pollack, J. B., R. M. Haberle, J. Schaeffer, and H. Lee 1990. Simulations of the general circulation of the Martian atmosphere, 1, Polar processes. *J. Geophys. Res.*, **95**, 1447–1473.

Pollack, J. B., R. M. Haberle, J. R. Murphy, J. Shaeffer, and H. Lee 1993*a*. Simulation of the general circulation of the martian atmosphere 2, Seasonnal pressure variations. *J. Geophys. Res.* **98**, 3149–3181.

Pollack, J. B., J. B. Dalton, D. Grinspoon, D. R. B. Wattson, R. Freedman, and D. Crisp 1993*b*. Near-infrared light from Venus nightside: A spectroscopic analysis. *Icarus* **103**, 1–42.

Pollack, J. B., M. E. Ockert-Bell, and M. K. Shepard 1995. Viking Lander image analysis of martian atmospheric dust. *J. Geophys. Res.* **100**, 5235–5250.

Rossow , W. B. 1978. Cloud microphysics: Analysis of the clouds of Earth, Venus, Mars, and Jupiter. *Icarus* **36**, 1–50.

Stansberry, J. A., R. M. Haberle, and C. P. McKay 1995. Paper presented at the 27th Annual Meeting of the Division for Planetary Science of the AAS, Hawaii, October 9, 1995.

Toon, O. B., J. B. Pollack, and C. Sagan 1977. Physical properties of the particles composing the martian dust storm of 1971-1972. *Icarus* **30**, 663–696.

Toon, O. B., C. P. McKay, T. P. Ackerman, and K. Santhanam 1989. Rapid calculation of radiative heating rates and photodissociation rates in inhomogeneous multiple scattering atmospheres. *J. Geophys. Res.* **94**, 16,287–16,301.

Van Leer , B. 1977. Towards the ultimate conservative difference scheme: IV. A new approach to numerical convection. *J. Computational Phys.* **23**, 276-299.

Washburn, E. 1948. *International critical tables of numerical data,physics, chemistry, and technology, volume 3*, McGraw Hill, New-York.

Wilson, R. W., 1997. A general circulation model of the martian polar warming. *Geophys. Res. Lett.* **24**, 123–126.

Wood, S. E., and D. A. Paige 1992. Modeling the martian seasonal CO_2 cycle: Fitting the Viking lander pressure curves. *Icarus* **99**, 1–14.

Wood, S. E., M. I. Richardson, and D. A. Paige 1996. A microphysical model of CO_2 snow on Mars. *Bull. Am. Astron. Soc.* **28**, 1064.